Electronic and magnetic properties of phosphorus across the first-order ferromagnetic transition of $(Mn,Fe)_2(P,Si,B)$ giant magnetocaloric materials

F. Guillou,* K. Ollefs, F. Wilhelm, and A. Rogalev
ESRF - The European Synchrotron Radiation Facility, 71 Avenue des Martyrs CS40220, F-38043 Grenoble Cedex 09, France

A. N. Yaresko
Max-Plank-Institut für Festkörperforschung, Heisenbergstrasse 1, D-70569 Stuttgart, Germany

H. Yibole, N. H. van Dijk, and E. Brück
FAME, TUDelft, Mekelweg 15, 2629JB Delft, The Netherlands

(Received 10 June 2015; revised manuscript received 26 November 2015; published 22 December 2015)

To study the evolution of the electronic states and magnetism of the metallic and metalloid atoms across the first-order ferromagnetic transition of $(Mn,Fe)_2(P,Si,B)$ compounds, x-ray absorption (XAS) and magnetic circular dichroism (XMCD) spectra were recorded at the K edges of P, Mn, and Fe. Surprisingly, while the Fe and Mn XAS spectra do not show pronounced changes, the K-edge XAS of P is strongly modified across the ferromagnetic transition and is a fingerprint of electronic structure changes at the phase transition. The evolution of the $3p$ electronic states of phosphorus is linked to changes in metal-metalloid bonding. The amplitude of this effect is correlated to the discontinuity in interatomic distances at the transition and progressively disappears with boron substitution. Moreover, it is found that the P atoms carry a finite magnetic moment in the ferromagnetic state in accordance with the results of band-structure calculations.

DOI: 10.1103/PhysRevB.92.224427 PACS number(s): 75.30.Sg, 75.30.Kz

I. INTRODUCTION

Even though first-order magnetic phase transitions (FOMTs) are scarce and represent only a limited fraction of the magnetic phase transitions, they are important for applications. The FOMTs have recently been the subject of a surge of interest due to their potential use in magnetic cooling. This magnetic refrigeration is based on the magnetocaloric effect (MCE) and can potentially replace the usual gas compression technique [1–3]. A MCE can be observed for all magnetic materials. However, it is greatly amplified when it occurs at a magnetic phase transition involving a latent heat, so that a FOMT leads generally to a giant MCE. The search for new MCE materials thus gives priority to those exhibiting a FOMT around room temperature. The various candidate refrigerants include FeRh [4], $Gd_5Si_2Ge_2$ [5], $La(Fe,Si)_{13}$ and its hydrides [6,7], Mn(As,Sb) [8], Heusler alloys [9], and MnFe(P,X) [10]. Among these systems, MnFe(P,X) is the most promising. The MnFe(P,X) alloys with X = As, Ge, Si, B are derived from the iron pnictide Fe_2P [10–13]. Their interest lays primarily in the large magnetocaloric effect in terms of isothermal entropy change (ΔS) and adiabatic temperature change (ΔT_{ad}), observed at the Curie temperature (T_C). Additionally, thanks to the possibility to vary the Mn/Fe ratio, the content and nature of the metalloid sites (P,X), these materials are highly tunable. For instance, the T_C can be adjusted over a broad temperature range, from 150 K up to more than 400 K, while maintaining a high MCE performance [12–14].

As it is of great interest for further developments, many efforts have been spent to describe and understand the FOMT in the various families of giant MCE materials. In most cases, it turns out that the FOMT originates from complex mechanisms combining a simultaneous evolution of the magnetic, structural, and electronic properties. In $Gd_5Si_2Ge_2$, x-ray absorption spectroscopy (XAS) and more specifically magnetic circular dichroism (XMCD) experiments have revealed that the elements Ge and Si play a key role in the magnetostructural transition due the development of induced magnetic moments on Ge and Si in the ferromagnetic state [15]. In $La(Fe,Si)_{13}$, the FOMT is expected to arise from the existence of several shallow minima in the energy-magnetization dependence, which results in a series of discontinuous transitions [16–18]. In FeRh, the mechanism responsible for the FOMT is still controversial, but the strong hybridization between Fe and Rh is an important factor, as well as the instability of the Rh magnetic moment at the FOMT [19,20].

For MnFe(P,X) materials, the FOMT and giant MCE are also expected to arise from an interplay between magnetic, structural, and electronic properties. The structure is represented in Fig. 1. MnFe(P,X) compounds have a hexagonal Fe_2P-type structure with two inequivalent metallic sites: a pyramidal $3g$ site for Mn and a tetrahedral $3f$ site for Fe. The nonmetallic elements occupy two inequivalent sites: a $2c$ site in the Fe layer and a $1b$ site in the Mn layer. The distribution of P/Si atoms between the $2c$ and $1b$ sites is random for Si $\approx 1/3$. However, at higher Si content or for other elements, a site preference starts to develop, where the largest atom has the tendency to occupy the $2c$ site [21]. A special aspect of the ferromagnetic transition in this system, observed in powder x-ray- and neutron-diffraction experiments, is that the FOMT is not associated with a change in crystal symmetry. The isostructural FOMT manifests itself by large changes in the lattice parameters with a discontinuity in the c/a ratio up to 8% [22,23]. This results in large changes in the metal-metalloid distances, with opposite directions for $2c$ and $1b$ sites; see Fig. 1. According to theoretical studies, a second

*francois.guillou@esrf.fr

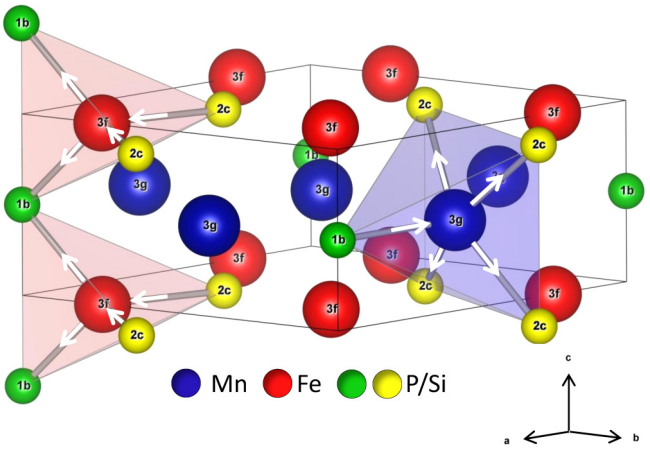

FIG. 1. (Color online) Schematic representation of the MnFe(P,Si) unit cell in the ferromagnetic state. The arrows mark the evolution of the metal-metalloids distances across the ferromagnetic transition (upon warming).

unusual facet is a change in the magnetic moment of Fe that takes place at the FOMT, and which is accompanied by a redistribution of electron density around Fe at the $3f$ site [12]. This scenario has led to a description of the FOMT as a competition between the formation of magnetic moments and chemical bonds [12,22]. It is worth noting that the same mechanism has been considered for the parent phase Fe_2P by using various theoretical approaches [24–27]. However, recent XMCD experiments carried out at the Mn and Fe $L_{2,3}$ edges of $MnFe_{0.95}P_{0.582}Si_{0.34}B_{0.078}$ and $Mn_{1.25}Fe_{0.7}P_{0.5}Si_{0.49}B_{0.01}$ show that the predicted change in the magnetic moment at the FOMT is overestimated [28].

Until now the possible role of the nonmetallic elements P and X = As, Ge, Si, B in the ground-state magnetic properties and the FOMT mechanism of MnFe(P,X) materials has received little attention. Substitutions of P by other elements are however known to have a significant influence on the properties, for instance by leading to a swift reduction of the latent heat in MnFe(P,Si,B) [23]. In this work, we aim to gain insight into the mechanism of the FOMT by focusing our attention on the electronic and magnetic properties of Fe, Mn and more especially on the nonmetallic element P. For that purpose, an element-specific probe such as XAS/XMCD combined with band-structure calculations is particularly appropriate. This study is carried out at the K edges of P, Mn, and Fe on a series of three $MnFe_{0.95}P_{0.66-x}Si_{0.34}B_x$ compositions. The $x = 0$ material is the most archetypical, as this composition shows the most pronounced FOMT (latent heat, c/a discontinuity, hysteresis) in the MnFe(P,X) system. At higher boron contents ($x = 0.040$ and 0.075), the FOMT progressively fades in the direction of a continuous transition, which allows one to track the XAS/XMCD evolutions at the FOMT as a function of the strength of the ferromagnetic transition.

II. EXPERIMENTAL AND CALCULATION METHODS

A fresh batch of $MnFe_{0.95}P_{0.66-x}Si_{0.34}B_x$ polycrystalline materials was produced according to the solid-state reaction method used during previous studies [13,14,23]. Powder x-ray diffraction, differential scanning calorimetry, and magnetization measurements were carried out to characterize the samples. The chemical and physical properties of this new batch are very close to those usually observed for this range of compositions [13,14,23]. To remove the ageing effects due to the FOMT, the samples were thermally cycled five times between liquid N_2 and room temperature. The x-ray absorption measurements were carried out on pellets of polycrystalline material.

XAS and XMCD measurements were performed at the ID12 beamline of the European Synchrotron Radiation Facility, France [29]. The source was the helical undulator Helios-II. The x-ray absorption spectra at the K edges of P, Mn, and Fe were recorded using the total fluorescence yield detection mode in backscattering geometry. For XMCD measurements, x-ray absorption spectra were collected consecutively for right and left circularly polarized x rays with the external magnetic field flipped between -0.9 and 0.9 T at each energy point (magnetic field applied along the beam direction). An applied magnetic field of 0.9 T allows reaching the saturation magnetization at temperatures below 50 K. Six spectra were recorded for each helicity and averaged. The XAS and XMCD spectra presented hereafter were corrected for self-absorption effect by assuming semi-infinite samples, but taking into account the various contributions (fluorescence of subshells and matrix as well as coherent and incoherent scattering), the angle of incidence of the x-ray beam, and the solid angle of the detector.

The experimental data of $MnFe_{0.95}P_{0.66}Si_{0.34}$ are compared with the theoretical XAS and XMCD spectra of chemically ordered $MnFeP_{2/3}Si_{1/3}$ crystal calculated using the fully relativistic Dirac linear muffin-tin orbital band-structure method (PY-LMTO package) [30]. For the ferromagnetic case, the calculations were performed on the basis of the experimental crystalline data for $MnFe_{0.95}P_{0.67}Si_{0.33}$ ($x_{3g} = 0.593$, $x_{3f} = 0.254$, $a = 6.167$ Å, and $c = 3.291$ Å) whereas for the calculations of the paramagnetic state, the experimental lattice parameters of $MnFe_{0.95}P_{0.67}Si_{0.33}$ at 310 K have been used ($a = 6.011$ Å, $c = 3.484$ Å, x_{3f}, and x_{3g} identical to the ferromagnetic phase) [23]. The structure was not relaxed and no empty spheres were inserted. We used the Perdew-Wang exchange-correlation potential [31]. Brillouin-zone (BZ) integrations were performed using the improved tetrahedron method and charge was obtained self-consistently on a grid of 450 k points in the irreducible part of the BZ. The basis consisted of transition metal s, p, d, f and metalloid s, p, d LMTOs. For the phosphorus XAS and XMCD spectra, the finite lifetime of a core hole is accounted for by a convolution with a Lorentzian of 0.6 eV width. For the simulation of XAS spectra, an averaging was performed to reflect the random orientation of the crystallographic axes with respect to the x-ray beam. XMCD spectra were simulated with the magnetization oriented along different crystallographic axes (a,b,c) and averaged.

III. RESULTS AND DISCUSSION

The magnetization as a function of temperature measured on superconducting quantum interference device magnetometer for the $MnFe_{0.95}P_{0.66-x}Si_{0.34}B_x$ materials is presented in

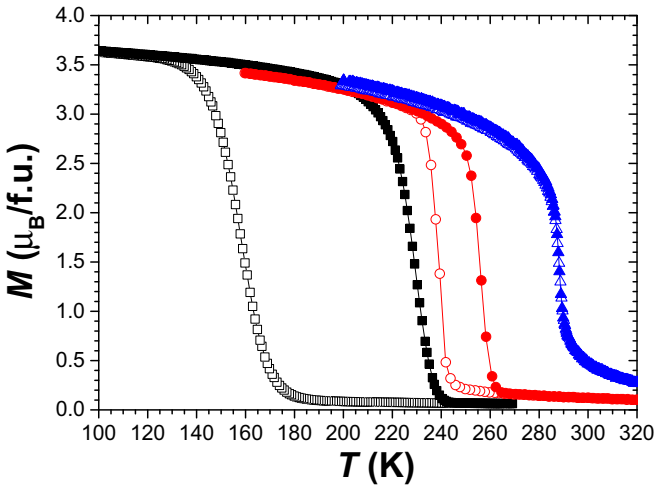

FIG. 2. (Color online) Magnetization as a function of the temperature measured upon cooling (open symbols) and heating (filled symbols) at $B = 1$ T for $MnFe_{0.95}P_{0.66-x}Si_{0.34}B_x$ compounds with $x = 0$ (squares), 0.040 (circles), and 0.075 (triangles).

Fig. 2. The overall behavior of the $M_B(T)$ curves is similar to those previously reported [13,23]. The $x = 0$ composition displays a T_C of 229 K upon warming and a large thermal hysteresis of more than 70 K. Increasing the boron content progressively shifts the T_C towards higher temperatures and weakens the first-order character of the ferromagnetic transition, which results in a progressive disappearance of the hysteresis. For the $x = 0$ material, a $M_T(B)$ curve has been recorded at $T = 5$ K and shows a saturation magnetization of about $4.1\mu_B$/f.u. This value agrees well with previous experimental reports [13,22].

Figure 3 shows the XAS and XMCD spectra at the K edge of Mn and Fe for $MnFe_{0.95}P_{0.66}Si_{0.34}$ sample. These data are in many aspects complementary to the recent investigation of MnFe(P,Si,B) materials in the soft x-ray range [28]:

(a) The electronic states being probed are different. In the previous study, the $L_{2,3}$ edge corresponds to a formally allowed electric-dipole transition ($2p \rightarrow 3d$) in Mn and Fe. As a result, the application of the sum rules to the XMCD spectra allows one to estimate the orbital and spin magnetic moments of the $3d$ states of transition metals. Here, the K-edge spectra are mostly dominated by the excitation of a $1s$ electron to unoccupied $4p$ states. The XMCD signal at the K edge, if one neglects quadrupolar transitions from $1s \rightarrow 3d$ states, reflects the orbital polarization of the $4p$ states. It originates from the spin-orbit interaction in the $4p$ band being magnetically polarized by the exchange with the $3d$ states. Thus, although the K-edge XMCD signal is only an indirect probe of the magnetism of $3d$ transition metals, it is proportional to the magnetization of the $3d$ states.

(b) The probing depth at the K edge is considerably larger than the escape depth of electrons that are usually used for detection of XAS and XMCD spectra at the L edges of $3d$ transition metals. Accordingly, the present data are representative of the bulk, which is of importance to study a FOMT presenting a large magnetoelastic effect. Additionally, the data at the K edge are practically unaffected by the presence of an oxide layer on the surface whereas it might give a strong contribution in the soft x-ray range.

(c) The MnFe(P,Si) composition with Mn/Fe ≈ 1 and Si $\approx 1/3$ shows an intense FOMT, and consequently, it presents

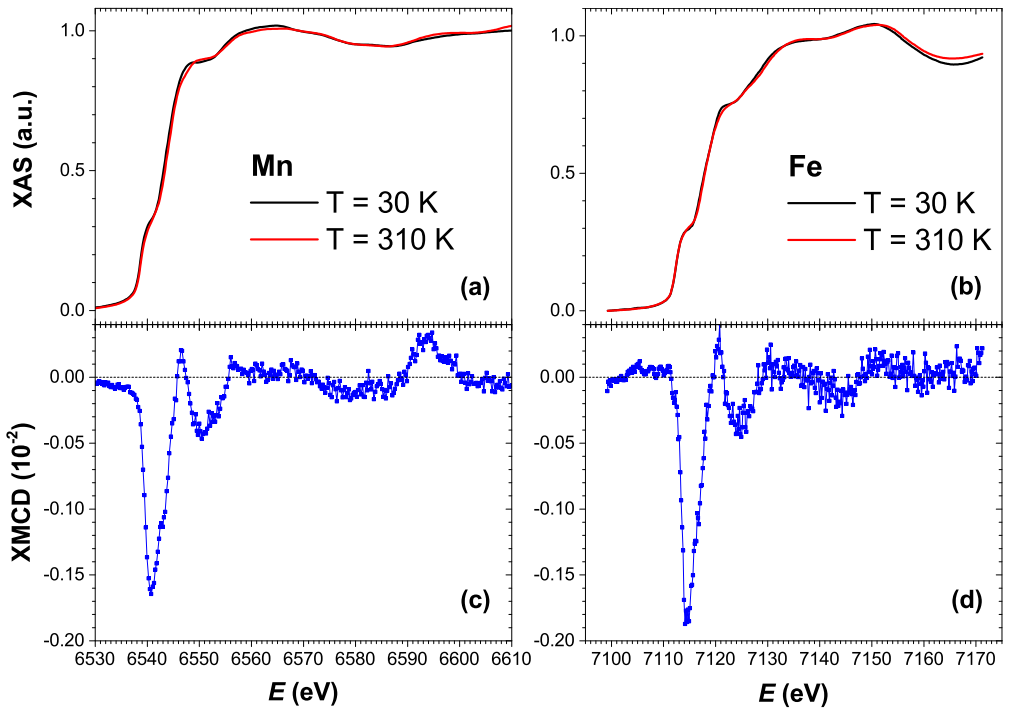

FIG. 3. (Color online) (a),(b) XAS spectra for $MnFe_{0.95}P_{0.66}Si_{0.34}$ at $T = 30$ K (black) and 310 K (red) for the K-edge of Mn and Fe, respectively. (c),(d) XMCD spectra for $MnFe_{0.95}P_{0.66}Si_{0.34}$ at $T = 30$ K and $B = 0.9$ T for the K-edge of Mn and Fe, respectively. The XMCD signal is normalized to the edge jump.

itself only in powder form, which requires a bulk sensitive technique. The previous study on $MnFe_{0.95}P_{0.582}Si_{0.34}B_{0.078}$ was representative of the most promising MCE composition that can be made in bulk polycrystalline form. The present study focuses on the $MnFe_{0.95}P_{0.66-x}Si_{0.34}B_x$ including $x = 0$, which shows a latent heat of about four times larger than the former and is thus more suitable to probe the signatures of the FOMT.

(d) The present study is performed over a large temperature range, more than 80 K below and above T_C for the $x = 0$ composition, which ensures that the measurement extends to outside the tails of the FOMT.

The K-edge XAS spectra of Mn and Fe for $MnFe_{0.95}P_{0.66}Si_{0.34}$ are presented in Figs. 3(a) and 3(b) for two temperatures, below and above the FOMT. Surprisingly, the spectra at both Mn and Fe K edge are found to be temperature independent, in particular in the vicinity of the edge. On the high-energy side of the spectra at both Mn and Fe K edges, one could observe some differences in amplitude and frequency of the extended x-ray absorption fine structure (EXAFS) wiggles which are related to the large changes in the lattice parameters at the FOMT. Another noticeable feature of the spectra is the absence of pre-edge structures, but rather two or three not well-defined shoulders on the rising edge. This kind of spectra is characteristic of the metallic nature of the absorbing atoms, i.e., Mn and Fe. The remarkable similarity of the XAS spectra across the FOMT indicates that there is no valence change for both transition metals, and their respective first coordination shells remain similar. The XMCD spectra at the Mn and Fe K-edge recorded below the FOMT are shown in Figs. 3(c) and 3(d). They present a dispersion-type profile with a pronounced negative peak in the rising part of the edge, followed by smaller bumps. The maxima of the XMCD signals are of the order of 10^{-3} of the edge jump for both Mn and Fe. Their integration leads to finite negative values in both cases, which indicates that the orbital moments are not completely quenched. The similar integrated values of XMCD spectra at the Mn and the Fe K edges and the fact that the probability of the quadrupolar transitions is about the same for both atoms suggest that the orbital moments carried by these atoms are comparable. The values of the calculated magnetic moments are presented in the following.

In Fig. 4, the XAS and XMCD spectra at the phosphorus K edge are presented for $MnFe_{0.95}P_{0.66}Si_{0.34}$. At room temperature, the energy of the edge is comparable to that for red phosphorus and significantly lower than that of the phosphates [32]. The overall XAS spectral shape resembles those observed for other M_2P metal phosphides [33]. After the main peak (A), which corresponds to the dipole allowed $1s \rightarrow 3p$ transition, a secondary feature (B) is observed 8 eV above the main peak. Two interpretations have been proposed for this secondary B peak: (i) multiple scattering resonance or (ii) a transition from a $1s$ electron into a conduction state involving mixing of the phosphorus $3p$ states and metal $4p$ bands. In contrast to Fe_2P, where a feature was found 6 eV below the edge [33], we do not observe any pre-edge peak for MnFe(P,Si,B) materials.

Let us now consider the K-edge spectrum of P at low temperatures. The shape of the B peak barely evolves upon cooling as its maximum only shows a minor shift of 0.4 eV to higher energies with a minor decrease in intensity. The

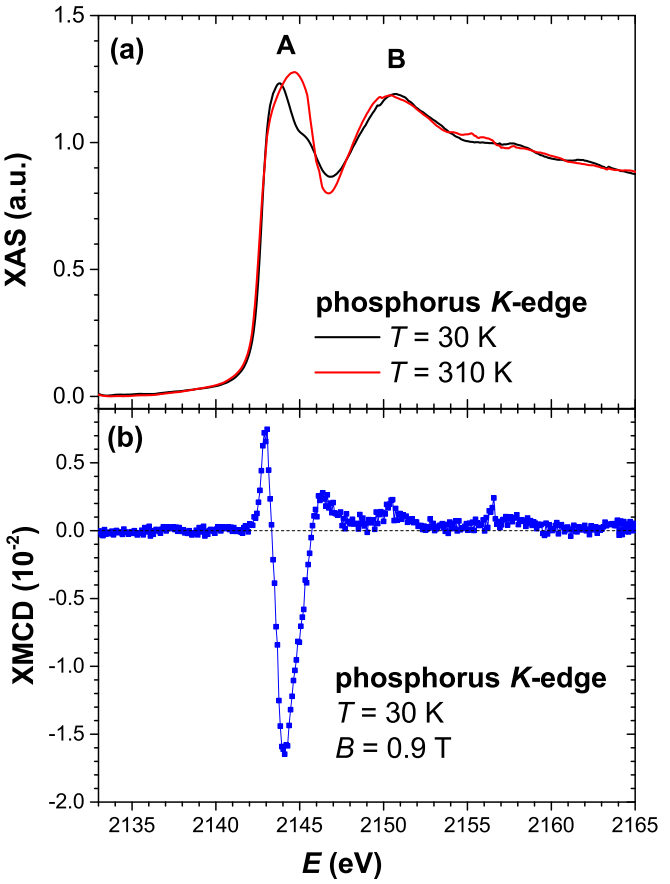

FIG. 4. (Color online) K-edge of P for $MnFe_{0.95}P_{0.66}Si_{0.34}$: (a) XAS spectra at $T = 30$ K and 310 K. (b) XMCD spectrum at $T = 30$ K and $B = 0.9$ T, normalized to the edge jump.

main large peak A is however strongly affected by the FOMT. Upon cooling, it seems that the peak A splits in two: the broad most intense peak at RT is getting weaker, whereas two others on either side appear to be clearly seen. The absence of a significant shift in energy of the P K edge allows us to suggest that also in the case of phosphorus, the FOMT does not lead to a valence change. But, the FOMT strongly affects the electronic structure of the phosphorus $3p$ states in the vicinity of the Fermi level. Some changes in the number of $3p$ holes and consequently $3p$ electrons are clearly seen in the spectra shown in Fig. 5 for various concentrations of boron. It is certainly much less than one hole per atom, but to quantify the observed changes is hardly possible at present.

The phosphorus K-edge XMCD spectrum recorded at low temperature is shown in Fig. 4(b). A very intense XMCD signal of 1.6% with respect to the edge jump is observed; this maximum is about ten times larger than that of Mn or Fe. This provides evidence that although P atoms are generally nonmagnetic, the $3p$ states of P in $MnFe_{0.95}P_{0.66}Si_{0.34}$ are magnetically polarized in the ferromagnetic state. An XMCD signal of induced nature on a metalloid element is not uncommon in ferromagnetic intermetallic alloys. It has for instance been observed on Si in Fe_3Si [34], on S in EuS and Fe_7S_8 [35,36], and on As in (Ga,Mn)As [37]. However, we are not aware of any attempt to measure magnetic polarization of $3p$ states of phosphorus. An XMCD signal on metalloid

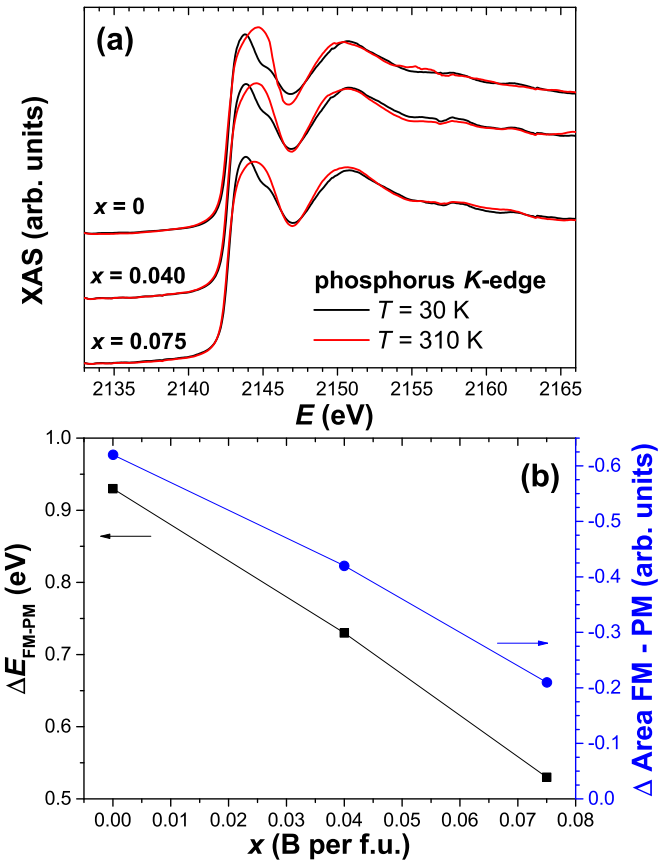

FIG. 5. (Color online) (a) XAS spectra at the K edge of P for $MnFe_{0.95}P_{0.66-x}Si_{0.34}B_x$ with $x = 0$, 0.040, and 0.075 at $T = 30$ and 310 K. (b) Evolution of the XAS spectra across the ferromagnetic transition as a function of the boron content: difference in the energy position of the peak A between 30 and 310 K (squares, left axis) and difference in the integral of XAS spectra recorded at $T = 30$ K and 310 K (circles, right axis). The range of integration is chosen between 2140 and 2152 eV.

elements is generally attributed to the polarization of the metalloid p states due to the hybridization with the metal $3d$ states (or a combination of p-d and p-f hybridization when rare earths are involved). For the P K edge, the integrated intensity of the XMCD spectrum, as in the case of transition metal, is proportional to the magnitude of the orbital moment induced in the $3p$ band. The integration of the XMCD intensity of the curve in Fig. 4(b) leads to a finite value, which is, however, slightly smaller than that of Fe or Mn in Fig. 3. Important to note that the sign of the orbital moment on the phosphorus is the same as on transition metals.

To study the influence of the strength of the FOMT on the $3p$ states of phosphorus, we have recorded the XAS spectra in the ferromagnetic and paramagnetic states for a series of samples $MnFe_{0.95}P_{0.66-x}Si_{0.34}B_x$ with $x = 0$, 0.040, and 0.075. These results are shown in Fig. 5(a). One can clearly see that the changes in peak A caused by the FOMT progressively decrease with the increase in the boron content, which corresponds to a weakening of the FOMT. To highlight this evolution as a function of x in $MnFe_{0.95}P_{0.66-x}Si_{0.34}B_x$, two parameters are used in Fig. 5(b): (i) the energy difference in the first maximum of the XAS spectra between the ferromagnetic and paramagnetic phase shows an almost linear decrease with x; and (ii) the area of the difference between the ferromagnetic and paramagnetic XAS spectra presents a decrease by a factor 3. It is interesting to note that this factor is relatively close to that observed for the reduction of the latent heat with boron substitution (about four times), which indicates that the changes in the phosphorus XAS spectra are directly related to the mechanism responsible of the FOMT in the MnFe(P,Si,B) system.

TABLE I. Spin (m_S) and orbital (m_L) magnetic moments of the $3d$ states of Fe and Mn and $3p$ states of P and Si calculated at $T = 0$ K for the three scenarios of metalloid occupancy: (i) $MnFeP_{2/3}Si_{1/3}$ (Si on half the $2c$ sites), (ii) $MnFeP_{2/3}Si_{1/3}$ (Si on $1b$), and (iii) $MnFeP_{1/3}Si_{2/3}$ (Si on $2c$).

Sites	(i) (μ_B)	(ii) (μ_B)	(iii) (μ_B)
Fe $3f$ ($m_S + m_L$)	1.471	1.493	1.522
m_S	1.439	1.464	1.487
m_L	0.032	0.029	0.035
Mn $3g$ ($m_S + m_L$)	2.905	2.945	2.801
m_S	2.881	2.921	2.776
m_L	0.024	0.024	0.025
P $2c$ ($m_S + m_L$)	−0.124	−0.121	
m_S	−0.124	−0.121	
m_L	10^{-4}	10^{-4}	
Si $2c$ ($m_S + m_L$)	−0.121		−0.129
m_S	−0.121		−0.129
m_L	-10^{-4}		-10^{-4}
P $1b$ ($m_S + m_L$)	−0.047		−0.063
m_S	−0.047		−0.063
m_L	10^{-4}		10^{-4}
Si $1b$ ($m_S + m_L$)		−0.063	
m_S		−0.063	
m_L		10^{-4}	

To get more insight into the experimental XAS and XMCD spectra at the K edge of phosphorus, $3p$ density of states of phosphorus were calculated using fully relativistic LMTO. A comparison with the experimental spectra allowed us to estimate the magnetic moment carried by phosphorus and propose an interpretation for the XAS spectral changes at the transition. A random P/Si occupation of the $2c$ and $1b$ sites is not implemented. But, to test the influence of the P/Si occupations on the output of the calculations, three scenarios have been considered: (i) a $MnFeP_{2/3}Si_{1/3}$ composition with Si atoms occupying one-half of the $2c$ sites and $1b$ fully occupied by P; (ii) a $MnFeP_{2/3}Si_{1/3}$ composition with $2c$ sites fully occupied by P and $1b$ by Si; (iii) a $MnFeP_{1/3}Si_{2/3}$ composition with $2c$ sites fully occupied by Si and $1b$ by P. The calculated magnetic moments are shown in Table I. It turns out that, either for $2c$ or $1b$ positions, the calculated P moments appear relatively constant irrespective of the Si occupation. The main influence of the Si content and site occupation concerns the spin moment of the $3d$ states of Fe and Mn. The total magnetic moment for the three scenarios ranges 4.13–4.25μ_B/f.u. and are in agreement with the bulk magnetization measurements presented in Fig. 2. Scenario (i) is a reasonable approximation

for $MnFe_{0.95}P_{0.66}Si_{0.34}$ which allows one to estimate the P spectra at both the $2c$ and $1b$ sites: this scenario has been chosen as the most suitable for the discussions below. The orbital moments calculated for Mn and Fe are relatively close, which is observed in the experiments by comparing the XMCD spectra shown in Fig. 3.

The partial density of states, calculated for Fe, Mn, and P in the ferromagnetic state, is shown in Figs. 6(a) and 6(b). The overall behavior agrees with previous band-structure calculations in various $MnFe(P,X)$ materials and the parent phase Fe_2P [12,24–27]. The occupied part of the PDOS can be decomposed into three regions. The first from -14 to -11 eV consists mainly of the s states of P from both $2c$ and $1b$ sites. The bottom of the main valence band group is located at -7.5 eV. This band group is mainly formed by Fe and Mn $3d$ states as well as P and Si $3p$ states. A strong hybridization between the transition-metal d and metalloid p states is clearly observed. The empty Mn and Fe p and f states, and the P/Si d states are situated well above the Fermi level (not shown). At the close vicinity of the Fermi level, we observe that for both the $2c$ and $1b$ sites, the p states of P form two structures in the bottom part of the conduction band at 1 and 3 eV. There is also a very broad maximum centered at about 7 eV above E_F. The partial DOS of phosphorus thus reflects the shape of the XAS spectrum shown in Fig. 4(a). Peak A is dominated by the transitions into phosphorus p states, which form antibonding states with the $3d$ transition-metal states, whereas peak B corresponds to transitions into the p states forming the broad maximum at 7 eV above E_f. The nonmagnetic partial density of states, calculated for Mn, Fe, and P with the paramagnetic structure, is presented in Figs. 6(c) and 6(d). The overall picture remains similar, with however a shift to higher energy of the antibonding transition-metal $3d$ and metalloid p states, as well as an increase in density of the phosphorus p states in the $1b$ site at about 3–4 eV. Such an energy shift of the antibonding states can also be seen on the partial DOS of the transition-metal d states in previous studies [12,27].

The evolution of the phopshorus K-edge XAS spectra in Fig. 4(a) could accordingly be explained by the energy shift of the antibonding metal-metalloid states associated with the large variation in interatomic distances and $\Delta(c/a)$ at the FOMT. For the $3g$ pyramidal site occupied by Mn, an expansion of the $3g$-$2c$ distance occurs upon heating from 2.491 to 2.521 Å, associated with it is a more pronounced shrinkage of the $3g$-$1b$ distances, from 2.510 to 2.446 Å. For the $3f$ tetrahedron site occupied by Fe, a simultaneous evolution of the $3f$-$2c$ and $3f$-$1b$ distances also occurs, a shrinkage of the $3f$-$2c$ distance by 0.06 Å of similar amplitude with the expansion of the $3f$-$1b$ distance by 0.05 Å [23]. This evolution leads to a permutation of the shortest Fe($3f$)-P and Mn($3g$)-P distance, resulting in a different distortion of the tetrahedral $3f$ site. The average Fe($3f$)-P($2c$ and $1b$) distance is however not modified as noticed from EXAFS study [38]. It is interesting to look at the projected charges for each site presented in Table II. At low temperatures, the total charges for P are similar for the phosphorus in the $2c$ and $1b$ positions, amounting to about 4.81 and 4.82, respectively. In contrast, at room temperature, the charge is about 4.87 for the $2c$ site (a change of about $+0.06$ upon heating) and 4.77 for the $1b$ site (a change of about -0.05 upon heating). In the meantime, the metallic elements barely evolve. This indicates that the opposite evolution in the transition metals—metalloids distances leads to a charge

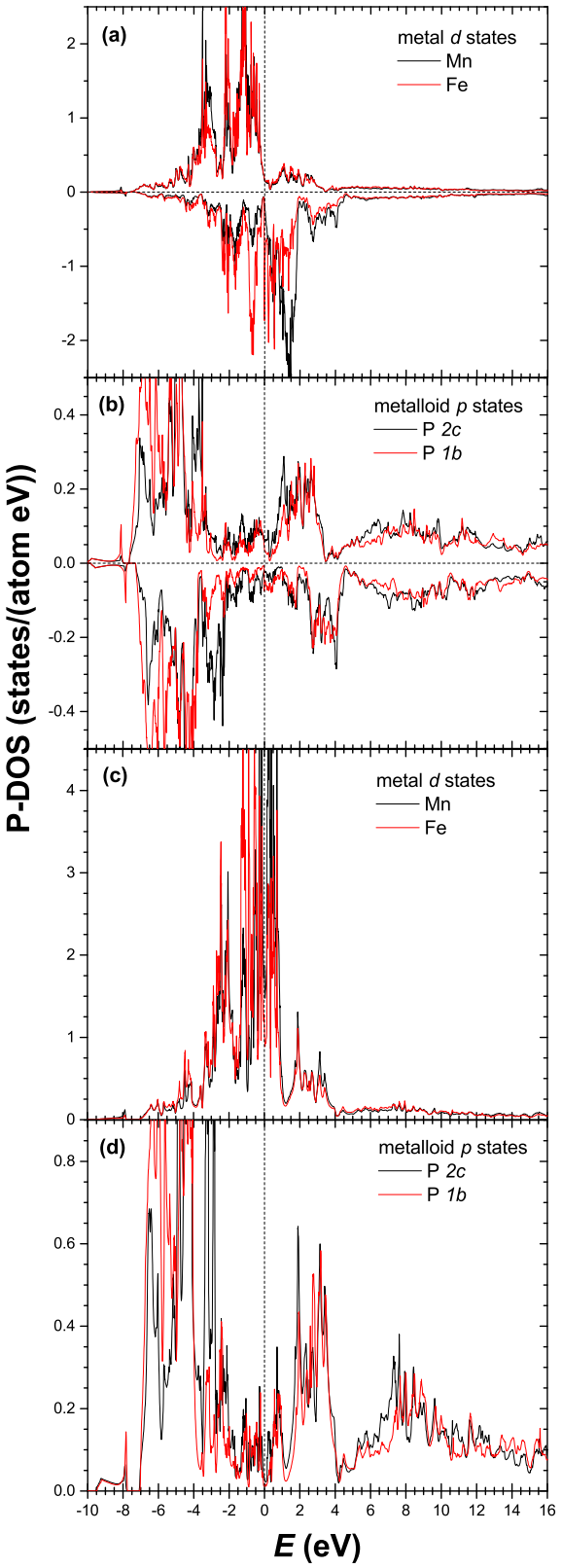

FIG. 6. (Color online) Partial densities of state for $MnFeP_{2/3}Si_{1/3}$ (i) in the ferromagnetic state (a),(b) and in a nonmagnetic state (c),(d).

TABLE II. Projected electron occupation numbers of the different sites calculated for $MnFeP_{2/3}Si_{1/3}$ (i) (nonpolarized calculations).

	Low temperature					Room temperature				
Atoms	*s*	*p*	*d*	*f*	Total	*s*	*p*	*d*	*f*	Total
Mn (3*g*)	0.541	0.858	5.883	0.122	7.404	0.542	0.859	5.871	0.119	7.391
Fe (3*f*)	0.467	0.666	6.614	0.057	7.804	0.459	0.659	6.621	0.057	7.796
P (2*c*)	1.457	2.801	0.550		4.808	1.459	2.829	0.578		4.866
Si (2*c*)	1.225	2.011	0.510		3.746	1.231	2.036	0.527		3.794
P (1*b*)	1.414	2.775	0.633		4.822	1.411	2.761	0.600		4.772

disproportion between P atoms in 2*c* and 1*b* sites. The evolution of the changes on the XAS phosphorus spectra as a function of the boron content shown in Fig. 5 supports a correlation with the changes in metal-metalloid distances, as the $\Delta(c/a)$ discontinuity at the FOMT is progressively reduced with the boron substitution [23]. This thus indicates that the charge redistribution among the phosphorus atoms, the energy shift of the hybridized transition-metal–metalloid states, and the resulting modification of the *K*-edge XAS spectra for phosphorous can be considered as a microscopic fingerprint of the FOMT.

The calculated *K*-edge XAS and XMCD spectra for the phosphorus atoms at the 2*c* and 1*b* positions are presented in Fig. 7. The spectra are simulated by considering a 2/3 and 1/3 weighted average for the contributions from the 2*c* and 1*b* sites, respectively. The contribution of each site is presented with a fixed Lorentzian broadening only. To take into consideration that at low energy the lifetime of the photoelectrons is only limited by the core-hole lifetime, while at high energy the mean-free path is limited by inelastic processes due to interaction with the electron gas of the system, the final curves were convoluted by an energy-dependent broadening function. When compared with the experimental spectrum from Fig. 4(b), the two main features of the XMCD curve are well reproduced by the calculations. The first positive peak combines equal contributions from 2*c* and 1*b* sites, whereas the main negative peak reaching an XMCD intensity of 1.6% mostly originates from the 2*c* site. The calculated XAS spectra for low temperature and room temperature are shown in Fig. 7(b). There is a clear similarity between the calculated and experimental XAS spectra presented in Fig. 4(a) on two aspects: the overall shape, the relatively narrow main peak is followed by a broader bump; the tilting of the main peak to higher energies across the transition is observed. The simulations indicate that the evolution of the XAS spectrum at the *K* edge of phosphorus across the FOMT originates from changes on both the 2*c* and 1*b* sites, with both sites showing a tilting of the A peak toward higher energies. The most noticeable contribution arises however from the 1*b* site with a gain in intensity about 4 eV above the edge. The rather encouraging agreement between the experimental and calculated XMCD spectra allows us to consider the results of the calculations shown in Table I as significant. The magnetic moments induced on P atoms are dominated by the spin moments of $-0.12\mu_B$ and $-0.05\mu_B$ for the 2*c* and 1*b* sites, respectively. The very small orbital moment calculated for both phosphorus sites is in line with the limited integral of the XMCD spectrum. It is interesting to note that induced moments of similar magnitude have also been predicted for P atoms in Fe_2P with calculated spin moments of about $-0.1\mu_B$ and $-0.05\mu_B$ for 2*c* and 1*b* sites, respectively [24,25]. In Table I, similar magnetic moments have been calculated for 2*c* and 1*b* sites irrespectively of the P or Si occupation. It is worthwhile to mention that induced moments of similar amplitude have also been calculated for As and Ge atoms in $MnFe(P,X)$ materials corresponding to the compositions presenting a giant MCE (not shown). The phosphorus *K*-edge XMCD signal in the paramagnetic phase was too weak to be measured at room

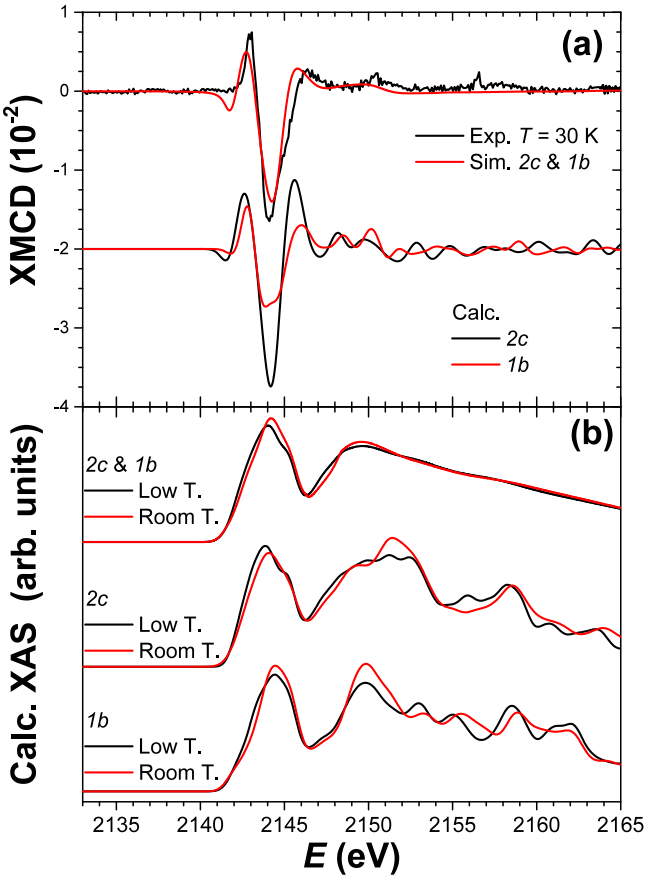

FIG. 7. (Color online) (a) Comparison between the calculated $MnFeP_{2/3}Si_{1/3}$(i) and experimental *K*-edge XMCD spectra of P for $MnFe_{0.95}P_{0.66}Si_{0.34}$ at $T = 30$ K and $B = 0.9$ T. (b) Calculated *K*-edge XAS spectra of P for the low-temperature and room-temperature states. The top curves correspond to a weighted average of 2*c* and 1*b* sites contributions (with an energy-dependent broadening). The two lower curves represent the contribution of each site (fixed Lorentzian broadening).

temperature and moderate magnetic field. It should however be noted that spin-polarized relativistic calculation predicts that a magnetic moment could also develop on phosphorus in the high-temperature crystalline structure. This suggests that an induced magnetism on the $2c$ and $1b$ sites is an intrinsic feature of this series of Fe_2P-type materials.

IV. CONCLUSIONS

The XAS and XMCD spectra at the K edges of P, Mn, and Fe in $MnFe_{0.95}P_{0.66-x}Si_{0.34}B_x$ materials with $x = 0$, 0.040, and 0.075 have been recorded in the ferromagnetic and paramagnetic states. For Mn and Fe, the similarity of the K-edge absorption spectra above and below the ferromagnetic transition indicates that the local electronic structure of transition metals are barely affected by the FOMT, as anticipated from the measurements performed at the $L_{2,3}$ edges of MnFe(P,Si,B) [28]. On the other hand, XAS and XMCD spectra at the phosphorus K-edge reveal a couple of unexpected features. In contrast to the Fe and Mn XAS spectra, pronounced changes are observed on the K-edge XAS spectrum of phosphorus across the ferromagnetic transition, which indicates an electronic reconstruction. This evolution is linked to the large changes in interatomic distances at the transition, upon heating, a shrinkage of the apex of the pyramidal $3g$ site (distance $3g$-$1b$), and a permutation of the shortest $3f$-metalloid distance, from $3f$-$2c$ in the ferromagnetic state to $3f$-$1b$ in the paramagnetic state, resulting in a different distortion of the Fe tetrahedron $3f$ site. These features and their consequences on the XAS spectra of P are reduced by the boron substitution. Although P atoms are considered to be nonmagnetic by nature, the XMCD spectrum shows that the $3p$ orbitals are magnetically polarized in the ferromagnetic phase. As expected, the corresponding orbital moment is parallel and smaller than those of the Mn or Fe $4p$ states. Band-structure calculations reproduce reasonably well the spectral shape and amplitude of the phosphorus dichroic signal and give spin moments of $-0.12\mu_B$ and $-0.05\mu_B$ for the P atoms in the $2c$ and $1b$ sites (below T_C), respectively. The polarization of the $3p$ states of P can be ascribed to hybridization with the Fe($3f$ site) and Mn($3g$ site) d states. We believe that our results unambiguously point out that phosphorus plays an important role in the first-order magnetic transition. This insight into the phase-transition mechanism should open new routes for the design of MnFe(P, X)-based giant magnetocaloric materials.

ACKNOWLEDGMENTS

The authors acknowledge the technical support provided by A. J. E. Lefering and P. Voisin at TU Delft and ESRF, respectively. Thanks are due to the European Synchrotron Radiation Facility for provision of synchrotron radiation. This work was supported by the Dutch Foundation for Fundamental Research on Matter (FOM) and BASF New Business.

[1] A. M. Tishin and Y. I. Spichkin, *The Magnetoclaoric Effect and its Applications* (Institute of Physics Publishing, Bristol, 2003).
[2] K. A. Gschneidner, Jr., V. K. Pecharsky, and A. O. Tsokol, Rep. Prog. Phys. **68**, 1479 (2005).
[3] A. Smith, C. R. Bahl, R. Bjørk, K. Engelbrecht, K. K. Nielsen, and N. Pryds, Adv. Energy Mater. **2**, 1288 (2012).
[4] M. P. Annaorazov, S. A. Nikitin, A. L. Tyurin, K. A. Asatryan, and A. K. Dovletov, J. Appl. Phys. **79**, 1689 (1996).
[5] V. K. Pecharsky and K. A. Gschneidner, Jr., Phys. Rev. Lett. **78**, 4494 (1997).
[6] F.-X. Hu, B.-G. Shen, J.-R. Sun, Z.-H. Cheng, G.-H. Rao, and X.-X. Zhang, Appl. Phys. Lett. **78**, 3675 (2001).
[7] A. Fujita, S. Fujieda, Y. Hasegawa, and K. Fukamichi, Phys. Rev. B **67**, 104416 (2003).
[8] H. Wada and Y. Tanabe, Appl. Phys. Lett. **79**, 3302 (2001).
[9] F.-X. Hu, B.-G. Shen, J.-R. Sun, and G.-H. Wu, Phys. Rev. B **64**, 132412 (2001).
[10] O. Tegus, E. Brück, K. H. J. Buschow, and F. R. de Boer, Nature (London) **415**, 150 (2002).
[11] N. T. Trung, Z. Q. Ou, T. J. Gortenmulder, O. Tegus, K. H. J. Buschow, and E. Brück, Appl. Phys. Lett. **94**, 102513 (2009).
[12] N. H. Dung, Z. Ou, L. Caron, L. Zhang, D. T. C. Thanh, G. A. de Wijs, R. A. de Groot, K. H. J. Buschow, and E. Brück, Adv. Energy Mater. **1**, 1215 (2011).
[13] F. Guillou, G. Porcari, H. Yibole, N. van Dijk, and E. Brück, Adv. Mater. **26**, 2671 (2014).
[14] F. Guillou, H. Yibole, G. Porcari, L. Zhang, N. H. van Dijk, and E. Brück, J. Appl. Phys. **116**, 063903 (2014).
[15] D. Haskel, Y. B. Lee, B. N. Harmon, Z. Islam, J. C. Lang, G. Srajer, Y. Mudryk, K. A. Gschneidner, and V. K. Pecharsky, Phys. Rev. Lett. **98**, 247205 (2007).
[16] M. D. Kuz'min and M. Richter, Phys. Rev. B **76**, 092401 (2007).
[17] A. Fujita and H. Yako, Scr. Mater. **67**, 578 (2012).
[18] M. E. Gruner, W. Keune, B. Roldan Cuenya, C. Weis, J. Landers, S. I. Makarov, D. Klar, M. Y. Hu, E. E. Alp, J. Zhao, M. Krautz, O. Gutfleisch, and H. Wende, Phys. Rev. Lett. **114**, 057202 (2015).
[19] J. Chaboy, F. Bartolomé, M. R. Ibarra, C. I. Marquina, P. A. Algarabel, A. Rogalev, and C. Neumman, Phys. Rev. B **59**, 3306 (1999).
[20] J. Kudrnovský, V. Drchal, and I. Turek, Phys. Rev. B **91**, 014435 (2015).
[21] X. F. Miao, L. Caron, P. Roy, N. H. Dung, L. Zhang, W. A. Kockelmann, R. A. de Groot, N. H. van Dijk, and E. Brück, Phys. Rev. B **89**, 174429 (2014).
[22] N. H. Dung, L. Zhang, Z. Q. Ou, L. Zhao, L. van Eijck, A. M. Mulders, M. Avdeev, E. Suard, N. H. van Dijk, and E. Brück, Phys. Rev. B **86**, 045134 (2012).
[23] F. Guillou, H. Yibole, N. van Dijk, and E. Brück, J. Alloys Compd. **632**, 717 (2015).
[24] H. Yamada and K. Terao, Phase Transit. **75**, 231 (2002).
[25] B. Wiendlocha, J. Tobola, S. Kaprzyk, R. Zach, E. K. Hlil, and D. Fruchart, J. Phys. D: Appl. Phys. **41**, 205007 (2008).
[26] X. Liu, J. P. Liu, Q. Zhang, and Z. Altounian, Phys. Lett. A **377**, 731 (2013).

[27] Z. Gercsi, E. K. Delczeg-Czirjak, L. Vitos, A. S. Wills, A. Daoud-Aladine, and K. G. Sandeman, Phys. Rev. B **88**, 024417 (2013).
[28] H. Yibole, F. Guillou, L. Caron, E. Jiménez, F. M. F. de Groot, P. Roy, R. de Groot, N. H. van Dijk, and E. Brück, Phys. Rev. B **91**, 014429 (2015).
[29] A. Rogalev, F. Wilhelm, J. Goulon, and G. Goujon, Springer Proc. Phys. **151**, 289 (2013).
[30] A. Perlov, A. Yaresko, and V. Antonov (unpublished).
[31] J. P. Perdew and Y. Wang, Phys. Rev. B **45**, 13244 (1992).
[32] G. Küper, J. Hormes, and K. Sommer, Macromol. Chem. Phys. **195**, 1741 (1994).
[33] P. E. R. Blanchard, A. P. Grosvenor, R. G. Cavell, and A. Mar, Chem. Mater. **20**, 7081 (2008).
[34] C. Antoniak, H. C. Herper, Y. N. Zhang, A. Warland, T. Kachel, F. Stromberg, B. Krumme, C. Weis, K. Fauth, W. Keune, P. Entel, R. Q. Wu, J. Lindner, and H. Wende, Phys. Rev. B **85**, 214432 (2012).
[35] A. Rogalev, J. Goulon, and C. Brouder, J. Phys.: Condens. Matter **11**, 1115 (1999).
[36] I. Letard, P. Sainctavit, and C. Deudon, Phys. Chem. Miner. **34**, 113 (2007).
[37] P. Wadley, A. A. Freeman, K. W. Edmonds, G. van der Laan, J. S. Chauhan, R. P. Campion, A. W. Rushforth, B. L. Gallagher, C. T. Foxon, F. Wilhelm, A. G. Smekhova, and A. Rogalev, Phys. Rev. B **81**, 235208 (2010).
[38] L. Yingjie, B. Huliyageqi, W. Haschaolu, Z. Song, O. Tegus, and I. Nakai, J. Electron. Spectrosc. Relat. Phenom. **196**, 104 (2014).